mathematics

MDPI

Article

Localized Method of Fundamental Solutions for Two-Dimensional Inhomogeneous Inverse Cauchy Problems

Junli Zhang [1], Hui Zheng [1,*], Chia-Ming Fan [2] and Ming-Fu Fu [1]

[1] School of Civil Engineering and Architecture, Nanchang University, Nanchang 330031, China; zhangjunli_@outlook.com (J.Z.); fumjngfu1958@outlook.com (M.-F.F.)
[2] Department of Harbor and River Engineering & Computation and Simulation Center, National Taiwan Ocean University, Keelung 20224, Taiwan; cmfan@ntou.edu.tw
* Correspondence: zhenghui@ncu.edu.cn

Abstract: Due to the fundamental solutions are employed as basis functions, the localized method of fundamental solution can obtain more accurate numerical results than other localized methods in the homogeneous problems. Since the inverse Cauchy problem is ill posed, a small disturbance will lead to great errors in the numerical simulations. More accurate numerical methods are needed in the inverse Cauchy problem. In this work, the LMFS is firstly proposed to analyze the inhomogeneous inverse Cauchy problem. The recursive composite multiple reciprocity method (RC-MRM) is adopted to change original inhomogeneous problem into a higher-order homogeneous problem. Then, the high-order homogeneous problem can be solved directly by the LMFS. Several numerical experiments are carried out to demonstrate the efficiency of the LMFS for the inhomogeneous inverse Cauchy problems.

Keywords: localized method of fundamental solutions; meshless method; recursive composite multiple reciprocity method; inhomogeneous problems; inverse Cauchy problems

MSC: 65D21

Citation: Zhang, J.; Zheng, H.; Fan, C.-M.; Fu, M.-F. Localized Method of Fundamental Solutions for Two-Dimensional Inhomogeneous Inverse Cauchy Problems. *Mathematics* **2022**, *10*, 1464. https://doi.org/10.3390/math10091464

Academic Editor: Ivo Petráš

Received: 23 March 2022
Accepted: 22 April 2022
Published: 27 April 2022

1. Introduction

The inverse Cauchy problem is well known for its numerically unstable characteristic; a small disturbance will lead to great errors in the numerical simulation. To develop a stable and accurate numerical method for the inverse Cauchy problem is very important. Different numerical methods are proposed and developed for solving the inverse Cauchy problems. One of the most popular methods for solving the inverse Cauchy problems is the finite element method (FEM), where the computational domain is divided into small meshes [1]. Similar to the FEM, the finite difference method (FDM) is also developed based on the mesh generation and has been used in inverse Cauchy problems [2]. However, these mesh-based methods have difficulties in the mesh generation when facing some complex geometry. Meanwhile, the boundary element method (BEM) has attracted some researchers' attention and has been utilized in the inverse Cauchy problems [3–5]. Since the fundamental solutions are employed in the BEM, the discretization is only imposed on the boundary, and the accuracy of the BEM is generally higher than other methods. However, the fundamental solutions in the BEM have some troubles in dealing with the singularities, and the BEM are not easy to apply to nonlinear problems.

Besides the mesh-based methods, many meshless methods have also been proposed for inverse Cauchy problems in recent years [6–9]. The collocation method is one type of the strong meshless methods, which are very popular recently for their simplicity [10,11]. Similar to the classification of the FEM and BEM, the collocation methods can be divided into domain-type and boundary-type methods. Domain-type collocation methods employ

interior nodes to discretize the governing equations. The boundary-type collocation methods employ the fundamental solutions or general solutions as the basis function, and the governing equations are analytically satisfied; thus, the accuracy of the boundary-type collocation methods is higher [12]. Many boundary-type collocation methods are developed for inverse Cauchy problems. For example, there are boundary-type methods available for inverse Cauchy problems including the boundary knot method (BKM) [13], the singular boundary method (SBM) [14], the boundary particle method (BPM) [15], and the method of fundamental solutions (MFS) [16,17].

The MFS was proposed by Karageorghis in 1964 [16] and has been utilized in different kinds of inverse Cauchy problems [17]. The MFS is powerful in dealing with engineering problems [18]; however, the full discretized matrix is always ill conditioned. Thus, the MFS is difficult to apply to the large-scale problems. Meanwhile, a finite difference approach is proposed into the global domain-type methods to localize the collocation methods [19,20], which makes the large-scale problems possible. Recently, the finite difference approach has been further applied to the MFS by considering the fictitious nodes [21], which is referred as the localized method of fundamental solutions (LMFS). Similar to the calculation process of the LRBFCM, the LMFS uses both of the interior nodes and boundary nodes at the same time to yield a sparse matrix. The LMFS can be applied to large-scale problems with higher accuracy than other domain-type methods. [22,23].

In general, the boundary-type methods cannot solve inhomogeneous PDEs directly. As such, several numerical techniques have been proposed to solve the inhomogeneous problems, such as the dual reciprocity method (DRM) [24,25], the multiple reciprocity method (MRM) [26,27], and the recursive composite multiple reciprocity (RC-MRM) technique [28]. The DRM and MRM solve the inhomogeneous problems by a linear combination of the homogeneous solution and the particular solution, and the accuracy is related to the approximation of the particular solutions. In order to avoid the errors caused by the particular solutions, the RC-MRM employs high-order differential operators to eliminate the inhomogeneous terms in the governing equations, so that the homogeneous problem can be solved by the LMFS directly. By using the RC-MRM, the accuracy of solving the inhomogeneous inverse Cauchy problem is only related to the numerical methods. The RC-MRM has been effectively applied to the Kirchhoff plate bending problems [29] and Winkler plate bending problems [30].

The paper is organized as follows: Section 2 mainly gives the details of numerical formation of the inhomogeneous inverse Cauchy problem. In Section 3, the RC-MRM is proposed to show how to eliminate the inhomogeneous terms in detail, and the numerical procedure of the LMFS is introduced clearly. In order to verify the effectiveness of this study, several numerical examples of 2D inhomogeneous inverse Cauchy problems are taken into consideration in Section 4. Finally, some conclusions and remarks are provided in Section 5.

2. The Inhomogeneous Inverse Cauchy Problem

In this section, the governing equation of the inverse problem is presented by a simple PDE given as follows,

$$\Re(u(\mathbf{x})) = f(\mathbf{x}),\ \mathbf{x} \in \Omega, \tag{1}$$

with boundary conditions

$$u(\mathbf{x}) = h(\mathbf{x}),\ \mathbf{x} \in \partial\Omega_1, \tag{2}$$

$$\frac{\partial u(\mathbf{x})}{\partial \mathbf{n}} = g(\mathbf{x}),\ \mathbf{x} \in \partial\Omega_1, \tag{3}$$

where $\Re()$ is a second-order differential operator, and $\mathbf{x} = (x, y)$ represents the spatial position of nodes. $f(\mathbf{x})$ is the inhomogeneous term of the governing equation. $h(\mathbf{x})$ and $g(\mathbf{x})$ are the Dirichlet boundary condition and Neumann boundary condition, respectively. As shown in Figure 1, Ω is the computational domain with boundary $\partial\Omega = \partial\Omega_1 \cup \partial\Omega_2 (\partial\Omega_1 \cap \partial\Omega_2 = \varnothing)$. In addition, $\mathbf{n} = (n_x, n_y)$ is the unit outward normal vector.

There is no information along boundary $\partial\Omega_2$ in the inverse problems. The main aim for the inverse Cauchy problem is to find out the numerical solutions of the unknown parts, including the boundary $\partial\Omega_2$ and the computational domain Ω.

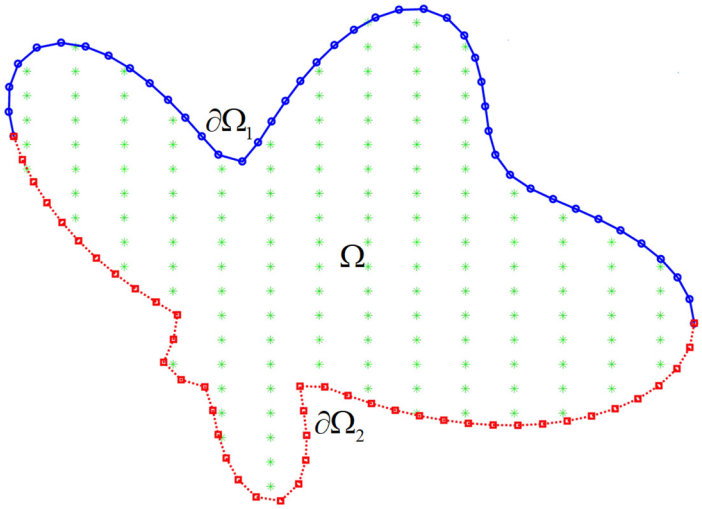

Figure 1. Schematic illustration for a computational domain.

3. Solution Procedure

In this section, the general idea of the RC-MRM and the details of the numerical discretization of the LMFS are presented.

3.1. The Recursive Multiple Reciprocity Technique (RC-MRM)

Since the fundamental solutions are evaluated from the homogeneous PDEs, the LMFS cannot be used directly to the inhomogeneous PDE. Therefore, the RC-MRM is applied to the LMFS to get the numerical solutions. The RC-MRM uses high-order differential operators to eliminate the inhomogeneous term $f(\mathbf{x})$ in the governing equations as follows:

$$L_M \cdots L_2 L_1 \Re(u(\mathbf{x})) = L_M \cdots L_2 L_1 \{(f(\mathbf{x}))\} \cong 0, \tag{4}$$

where $L_m (m = 1, 2, 3, \cdots, M.)$ denote some second-order differential operators, and M is the number of the differential operators that we used in Equation (4). The linear differential operators L_m in Equation (4) are not unique, we mainly consider the Laplacian $\Delta = \nabla^2 = \frac{\partial^2}{\partial x^2} + \frac{\partial^2}{\partial y^2}$, the Helmholtz operator $\Delta + \kappa^2$, and the modified Helmholtz operator $\Delta - \kappa^2$, where κ is the wavenumber. The above three differential operators can be used on both side of Equation (1) until the inhomogeneous term is eliminated.

Since the re-formulated homogeneous governing equation becomes a higher-order PDE, as shown in Equation (4), extra boundary conditions are added to ensure the uniqueness of the numerical solution. According to principle of the RC-MRM, additional M boundary conditions are given as follows,

$$\begin{cases} \Re(u(\mathbf{x})) = f(\mathbf{x}), & \mathbf{x} \in \partial\Omega, \\ L_1 \Re(u(\mathbf{x})) = L_1 f(\mathbf{x}), & \mathbf{x} \in \partial\Omega, \\ L_2 L_1 \Re(u(\mathbf{x})) = L_2 L_1 f(\mathbf{x}), & \mathbf{x} \in \partial\Omega, \\ \cdots & \cdots \\ L_{M-1} \cdots\cdots L_2 L_1 \Re(u(\mathbf{x})) = L_{M-1} \cdots\cdots L_2 L_1 f(\mathbf{x}), & \mathbf{x} \in \partial\Omega. \end{cases} \tag{5}$$

Therefore, the inhomogeneous problem described in Equations (1)–(3) can be changed to a higher-order homogeneous problem in Equation (4) with the boundary conditions described in Equations (2), (3) and (5). It should be noted that the new added boundary conditions are put along all the boundaries. Then, the homogeneous solution can be

obtained directly by the LMFS. In order to illustrate the specific operation process of the RC-MRM, we propose a simple example below. If the original inhomogeneous governing equation is $\Delta u = x + y$, when we set $L_1 = \Delta$, a new homogeneous governing equation $L_1 \Delta u = 0$ can be easily obtained. Moreover, the new boundary condition $\Delta u = x + y$ of the whole boundaries is added to ensure the uniqueness of the solution.

3.2. Introduction of the LMFS

Before introducing the LMFS, the fundamental solution is defined as G, which can be obtained according to the differential operators $\Re$ or L_m mentioned in Equations (1) and (4). Three fundamental solutions according to different differential operators can be found on the right side of Table 1 [31], where Y_0 and K_0 are the second kind of Bessel function and modified Bessel function, respectively. In addition, $r = \left\| \mathbf{x}_i - \mathbf{s}_j \right\|$ represents the distance between the i^{th} filed node $\mathbf{x}_i = (x_i, y_i)$ and the j^{th} source node $\mathbf{s}_j = \left(s_j^x, s_j^y \right)$, which can be found in Figure 2.

Table 1. Fundamental solutions of different differential operators in two-dimensional cases [31].

$\Re$ or L_m	G
Δ	$-\frac{1}{2\pi} \ln(r)$
$\Delta + \kappa^2$	$\frac{1}{4} Y_0(\kappa r)$
$\Delta - \kappa^2$	$\frac{1}{2\pi} K_0(\kappa r)$

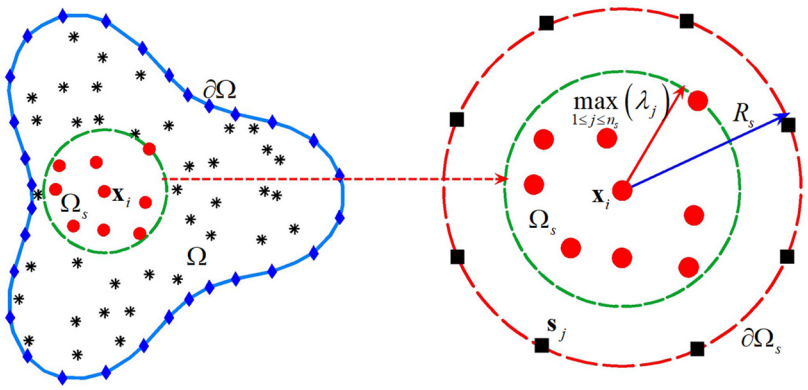

Figure 2. Schematic of a local domain Ω_s.

As shown in Figure 2, a local domain Ω_s near the i^{th} node is considered, where $(n_s - 1)$ can be found inside the local domain Ω_s. The numerical solutions of the nodes inside the local domain can be expressed by considering fictitious nodes uniformly distributed on an artificial circle $\partial\Omega_s$ as follows:

$$u(\mathbf{x}) = \sum_{j=1}^{n_s} \alpha_j G\left(\mathbf{x}, \mathbf{s}_j\right), \quad \mathbf{x} \in \Omega_s, \tag{6}$$

where $\left\{ \mathbf{s}_j \right\}_{j=1}^{n_s}$ are the fictitious source nodes uniformly distributed on an artificial circle $\partial\Omega_s$, as shown on the right side of Figure 2. $\left\{ \alpha_j \right\}_{j=1}^{j=n_s}$ are the unknown coefficients of source nodes, which are related to $\left\{ \mathbf{s}_j \right\}_{j=1}^{n_s}$. The radius of the artificial circle is defined as R_s, which can be controlled by the following equation,

$$R_s = R \times \max_{1 \le j \le n_s} \left(\lambda_j \right), \tag{7}$$

where λ_j is the distance between the i^{th} node and j^{th} nodes in the local domain, and $R > 1$ is usually called the scaling factor that can be given randomly in a considerable range. In this work, $R = 10$ is chosen for simplicity; thus, an artificial circle or surface centered at i^{th} node can be generated with radius R_s. Equation (6) can be rewritten as

$$\mathbf{u}_{n_s \times 1} = \mathbf{G}_{n_s \times n_s} \boldsymbol{\alpha}_{n_s \times 1}, \tag{8}$$

where

$$\mathbf{G}_{n_s \times n_s} = \begin{Bmatrix} G(\mathbf{x}_1, \mathbf{s}_1) & G(\mathbf{x}_1, \mathbf{s}_2) & \cdots & G(\mathbf{x}_1, \mathbf{s}_{n_s}) \\ G(\mathbf{x}_2, \mathbf{s}_1) & G(\mathbf{x}_2, \mathbf{s}_2) & \cdots & G(\mathbf{x}_2, \mathbf{s}_{n_s}) \\ \vdots & \vdots & \cdots & \vdots \\ G(\mathbf{x}_{n_s}, \mathbf{s}_1) & G(\mathbf{x}_{n_s}, \mathbf{s}_2) & \cdots & G(\mathbf{x}_{n_s}, \mathbf{s}_{n_s}) \end{Bmatrix}. \tag{9}$$

Then, the unknown coefficients at source nodes on the artificial circle $\partial\Omega_s$ can be interpolated in terms of the information at the n_s local nodes, which can be expressed as

$$\boldsymbol{\alpha}_{n_s \times 1} = \left(\mathbf{G}_{n_s \times n_s}\right)^{-1} \mathbf{u}_{n_s \times 1}. \tag{10}$$

Reconsidering Equation (10) back to Equation (16), the phase field at i^{th} node can be changed as follows,

$$u(\mathbf{x}_i) = \sum_{j=1}^{n_s} \alpha_j G\left(\mathbf{x}_i, \mathbf{s}_j\right) = \mathbf{c}_{1 \times n_s} \boldsymbol{\alpha}_{n_s \times 1} = \mathbf{c}_{1 \times n_s} \left(\mathbf{G}_{n_s \times n_s}\right)^{-1} \mathbf{u}_{n_s \times 1} = \sum_{j=1}^{n_s} W_j^i u_j, \tag{11}$$

where $\mathbf{c}_{1 \times n_s} = \begin{Bmatrix} G(\mathbf{x}_i, \mathbf{s}_1) & G(\mathbf{x}_i, \mathbf{s}_2) & G(\mathbf{x}_i, \mathbf{s}_3) & \ldots & G(\mathbf{x}_i, \mathbf{s}_{n_s}) \end{Bmatrix}$ is the vector related to the fundamental solution by considering $\mathbf{x}_i$ and $\mathbf{s}_j$. $\left\{W_j^i\right\}_{j=1}^{n_s}$ are the weighting coefficients of the n_s nodes in the local domain at the i^{th} node. By considering the sparse system of the weighting coefficients, the phase field inside domain is evaluated directly without knowing the unknown coefficients $\boldsymbol{\alpha}_{n_s \times 1}$ in the LMFS. This is different from the classical MFS.

Since $\mathbf{G}_{n_s \times n_s}$ is a full matrix during the computational process, the ill condition should be proper treated when dealing with the inverse of $\mathbf{G}_{n_s \times n_s}$. In this work, the MATLAB command *pinv* (**G**, *tol*) is directly taken to solve the inverse of $\mathbf{G}_{n_s \times n_s}$, where *tol* is the tolerance error. The command, *pinv* (**G**, *tol*), reduces the impact of the ill condition by using the singular value decomposition (SVD). Then, the representation of **G** becomes:

$$\mathbf{G} = \mathbf{U}\mathbf{S}\mathbf{V}^{\mathbf{T}} = \begin{bmatrix} \mathbf{U}_1 & \mathbf{U}_2 \end{bmatrix} \begin{bmatrix} \mathbf{S}_1 & 0 \\ 0 & 0 \end{bmatrix} \begin{bmatrix} \mathbf{V}_1 & \mathbf{V}_2 \end{bmatrix}^{\mathbf{T}}, \tag{12}$$

$$\mathbf{G} = \mathbf{U}_1 \mathbf{S}_1 \mathbf{V}_1^{\mathbf{T}}. \tag{13}$$

where **U** is a left singular matrix that contains eigenvectors of matrix GG^T, **V** is a right singular matrix that contains eigenvectors of matrix $G^T\mathbf{G}$, and **S** is a diagonal matrix containing singular values {\displaystyle \mathbf{U^{*}U} =\mathbf{V^{*}V} =\mathbf{I} _{r}}. When the singular values along the diagonal of **S** are smaller than *tol*, the pseudoinverse of **G** is then given by:

$$\mathbf{B} = \mathbf{V}_1 \mathbf{S}_1^{-1} \mathbf{U}_1^{\mathbf{T}}. \tag{14}$$

The MATLAB command **B** = *pinv* (**G**, *tol*) returns the Moore–Penrose pseudoinverse of matrix **G**. It should be noted that the pseudoinverse **B** exists for any matrix **G**, and **B** has the same dimensions as $\mathbf{G}^{\mathbf{T}}$.

Since Equation (11) is derived by assuming that the solution within the local domain of the i^{th} node satisfies the governing equation, each interior node can be taken as the i^{th}

node, and the procedures of Equations (6)–(11) can be implemented. Thus, the following system of linear algebraic equations can be yielded,

$$u(\mathbf{x}_i) - \sum_{j=1}^{n_s} W_j^i u_j = 0, \quad i = 1, 2, 3, \ldots, n_i \ . \tag{15}$$

Meanwhile, the Dirichlet boundary condition can be satisfied directly as follows,

$$u(\mathbf{x}_i) = h_i, \quad i = n_i + 1, n_i + 2, n_i + 3, \ldots, n_i + n_{b1} \ , \tag{16}$$

where n_i represents the number of interior nodes, and n_{b1} and n_{b2} represent the numbers of nodes located at boundary $\partial\Omega_1$ and boundary $\partial\Omega_2$, respectively. The Dirichlet boundary conditions are given on $\partial\Omega_1$, and there is no boundary information on $\partial\Omega_2$. $N = n_i + n_b$ is defined as the total number of the nodes, and $n_b = n_{b1} + n_{b2}$ is the number of boundary nodes. Since the Neumann boundary conditions are usually expressed as the first-order derivatives, the numerical approximation of the first-order derivative can be presented as

$$\left.\frac{\partial u}{\partial x}\right|_{\mathbf{x}_i} = \sum_{j=1}^{n_s} \alpha_j \left.\frac{\partial G\left(\mathbf{x}, \mathbf{s}_j\right)}{\partial x}\right|_{\mathbf{x}_i} = \mathbf{c}^{x,i}_{1 \times n_s} \boldsymbol{\alpha}_{n_s \times 1} = \mathbf{c}^{x,i}_{1 \times n_s} \left(\mathbf{G}_{n_s \times n_s}\right)^{-1} \mathbf{u}_{n_s \times 1} = \sum_{j=1}^{n_s} W_j^{x,i} u_j, \tag{17}$$

$$\left.\frac{\partial u}{\partial y}\right|_{\mathbf{x}_i} = \sum_{j=1}^{n_s} \alpha_j \left.\frac{\partial G\left(\mathbf{x}, \mathbf{s}_j^i\right)}{\partial y}\right|_{\mathbf{x}_i} = \mathbf{c}^{y,i}_{1 \times n_s} \boldsymbol{\alpha}_{n_s \times 1} = \mathbf{c}^{y,i}_{1 \times n_s} \left(\mathbf{G}_{n_s \times n_s}\right)^{-1} \mathbf{u}_{n_s \times 1} = \sum_{j=1}^{n_s} W_j^{y,i} u_j, \tag{18}$$

where

$$\mathbf{c}^{x,i}_{1 \times n_s} = \left\{ \left.\frac{\partial G\left(\mathbf{x}, \mathbf{s}_1\right)}{\partial x}\right|_{\mathbf{x}_i} \quad \left.\frac{\partial G\left(\mathbf{x}, \mathbf{s}_2\right)}{\partial x}\right|_{\mathbf{x}_i} \quad \left.\frac{\partial G\left(\mathbf{x}, \mathbf{s}_3\right)}{\partial x}\right|_{\mathbf{x}_i} \quad \cdots \quad \left.\frac{\partial G\left(\mathbf{x}, \mathbf{s}_{n_s}\right)}{\partial x}\right|_{\mathbf{x}_i} \right\}$$

and

$$\mathbf{c}^{y,i}_{1 \times n_s} = \left\{ \left.\frac{\partial G\left(\mathbf{x}, \mathbf{s}_1\right)}{\partial y}\right|_{\mathbf{x}_i} \quad \left.\frac{\partial G\left(\mathbf{x}, \mathbf{s}_2\right)}{\partial y}\right|_{\mathbf{x}_i} \quad \left.\frac{\partial G\left(\mathbf{x}, \mathbf{s}_3\right)}{\partial y}\right|_{\mathbf{x}_i} \quad \cdots \quad \left.\frac{\partial G\left(\mathbf{x}, \mathbf{s}_{n_s}\right)}{\partial y}\right|_{\mathbf{x}_i} \right\}$$

are the vectors of the derivatives of fundamental solutions. $\left\{W_j^{x,i}\right\}_{j=1}^{n_s}$ and $\left\{W_j^{y,i}\right\}_{j=1}^{n_s}$ are the weighting coefficients related to derivative calculation. By considering the formulation of first-order derivative in Equations (17) and (18), the Neumann boundary condition can be discretized as

$$n_{xi} \left.\frac{\partial u}{\partial x}\right|_i + n_{yi} \left.\frac{\partial u}{\partial y}\right|_i = n_{xi} \sum_{j=1}^{n_s} W_j^{x,i} u_j + n_{yi} \sum_{j=1}^{n_s} W_j^{y,i} u_j = g_i, \quad i = n_i + 1, n_i + 2, \ldots, n_i + n_{b1} \ , \tag{19}$$

where $\mathbf{n}_i = \left(n_{xi}, n_{yi}\right)$ is the unit outward normal vector at the i^{th} node. Mapping from the local to global domain, the governing equations in Equation (15) and the boundary conditions in Equations (16) and (19) can be recast as the following sparse system

$$\mathbf{A}_{N \times N} \mathbf{u}_{N \times 1} = \mathbf{b}_{N \times 1}, \tag{20}$$

where $\mathbf{A}$ is the coefficient matrix, while $\mathbf{b}$ is the vector consist of the forcing term related to the governing equations and boundary conditions. The numerical solution $\mathbf{u}_{N \times 1}$ can be obtained by solving the above sparse system. In this paper, a MATLAB command *backslash* is used to solve the above system [11].

4. Numerical Examples

In this section, several different inhomogeneous inverse Cauchy problems are presented to show the efficiency and stability of the proposed LMFS. Some noises are added

to the boundary conditions to show the ability of the proposed LMFS. The noise data are introduced as follows:

$$\hat{h}_l = h_l(1 + s\varepsilon_l), \tag{21}$$

$$\hat{g}_p = g_p(1 + s\varepsilon_p), \tag{22}$$

where ε_l and ε_p are random numbers between $[-1, 1]$, and l and p represent the index of the number of boundary nodes on the Dirichlet and the Neumann boundary, respectively, as shown in Figure 1. s is used to control the noise data, which are given by researchers. Since the noise is caused by boundary measurement and the additional boundary conditions are derived by the RC-MRM without any measurement, there is no need to consider the noise in the additional boundary conditions. It means that the boundary conditions presented in Equation (5) remain unchanged. The maximum average relative error E_{maxr} and global error E_{global} in this work are defined as follows:

$$E_{maxr} = max\left|\frac{u^a(\mathbf{x}_k) - u(\mathbf{x}_k)}{u^a(\mathbf{x}_k)}\right|, \tag{23}$$

$$E_{global} = \sqrt{\frac{\sum_{k=1}^{N}(u^a(\mathbf{x}_k) - u(\mathbf{x}_k))^2}{\sum_{k=1}^{N}(u^a(\mathbf{x}_k))^2}}. \tag{24}$$

where $u^a(\mathbf{x}_k)$ and $u(\mathbf{x}_k)$ are the analytical and numerical solutions at $\mathbf{x}_k$, respectively.

In order to find the optimal tolerance of MATLAB command *pinv*, the previous work by Wang et al. [32] is considered in this work, where $tol = 10^{-3}$ is used in Examples 2 and 4 while $tol = 10^{-4}$ is picked up for Examples 1 and 3. Since the LMFS can always get accurate results with a big range of R in the previous research [21], a fixed $R = 10$ is set in all the examples.

4.1. Example 1

In this example, a simple unit square domain is considered in Figure 3, where $\Omega = \{(x, y)|0 < x < 1, 0 < y < 1\}$ represents the interior domain, and $\Gamma_j, j = 1...4$ represents the four boundaries, respectively. The Dirichlet boundary conditions with noise data are considered on Γ_1, Γ_2, and Γ_3. There is no information on Γ_4, an additional Neumann boundary condition with noise data imposed on Γ_1 to guarantee the solvability of the system.

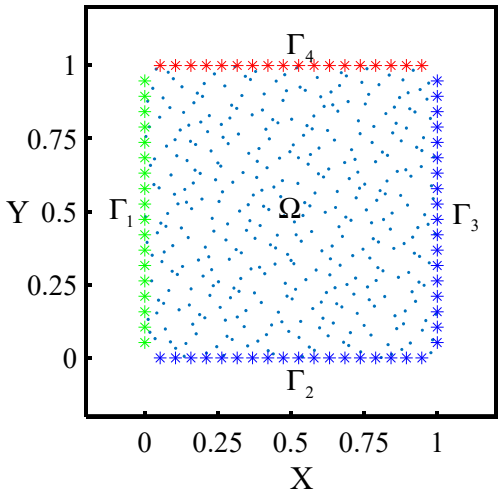

Figure 3. Collocation nodes' distribution.

The inhomogeneous governing equation subjected to mixed boundary conditions of Equations (2) and (3) is given as follows:

$$\Re(u(\mathbf{x})) = (\Delta - \kappa^2)u(\mathbf{x}) = f(\mathbf{x}), \quad \mathbf{x} \in \Omega, \tag{25}$$

where $\kappa = \frac{1}{2\pi}$ is utilized. The following analytical solution is considered,

$$u^a(\mathbf{x}) = 4(e^{\kappa x} + e^{\kappa y}) + \frac{\sin(\gamma x) + \cos(\gamma y)}{5} + \frac{x^3 + y^3}{2} + 5(x + y) - \frac{5}{2}, \tag{26}$$

where the constant γ=1 is simply used. The given boundary conditions without noise data can be obtained from Equation (26), which are presented as follows:

$$u(\mathbf{x}) = h(\mathbf{x}) = 4(e^{\kappa x} + e^{\kappa y}) + \frac{\sin(\gamma x) + \cos(\gamma y)}{5} + \frac{x^3 + y^3}{2} + 5(x + y) - \frac{5}{2}, \ \mathbf{x} \in \Gamma_1, \Gamma_2, \Gamma_3, \tag{27}$$

$$\frac{\partial u(\mathbf{x})}{\partial \mathbf{n}} = g(\mathbf{x}) = \left(4\kappa e^{\kappa x} + \frac{\cos(\gamma x)}{5} + \frac{3}{2}x^2 + 5\right)\mathbf{n}_x + \left(4\kappa e^{\kappa y} - \frac{\sin(\gamma y)}{5} + \frac{3}{2}y^2 + 5\right)\mathbf{n}_y, \ \mathbf{x} \in \Gamma_1. \tag{28}$$

When considering noise in Equations (21) and (22), the given boundary conditions in Equations (27) and (28) can be rewritten as

$$\hat{h}(\mathbf{x}) = h(\mathbf{x})(1 + s\varepsilon_l), \ \mathbf{x} \in \Gamma_1, \Gamma_2, \Gamma_3, \tag{29}$$

$$\hat{g}(\mathbf{x}) = g(\mathbf{x})(1 + s\varepsilon_p), \ \mathbf{x} \in \Gamma_1, \tag{30}$$

where ε_l and ε_p are random numbers between $[-1, 1]$, $l = 1, 2, \ldots, n_{b1} + n_{b2} + n_{b3}$ represents the index of number of boundary nodes on $\Gamma_1, \Gamma_2, \Gamma_3$, and $p = 1, 2, \ldots, n_{b1}$ represents the index of number of boundary nodes on Γ_1. In this paper, we chose s = 1%, 3%, 5%, and 7%. From Equations (25) and (26), the inhomogeneous forcing term can be expressed as,

$$f(\mathbf{x}) = -\frac{\kappa^2 + \gamma^2}{5}(\sin(\gamma x) + \cos(\gamma y)) + 3(x + y) - \kappa^2\left(\frac{x^3 + y^3}{2} + 5(x + y) - \frac{5}{2}\right) \tag{31}$$

Using the RC-MRM, the inhomogeneous term in the governing equation can be annihilated by three differential operators as

$$L_3L_2L_1 \ \Re(u(\mathbf{x})) = \Delta^2(\Delta + \gamma^2)(\Delta - \kappa^2)u(\mathbf{x}) = 0, \quad \mathbf{x} \in \Omega, \tag{32}$$

where $L_1 = \Delta + \gamma^2$ and $L_2 = L_3 = \Delta$. Since Equation (32) is an eighth-order homogeneous problem, the LMFS can be used directly. According to the procedure in RC-MRM, three additional boundary conditions are required to guarantee the solvability of the eighth-order PDE, which are given as

$$\Re(u(\mathbf{x})) = (\Delta - \kappa^2)u(\mathbf{x}) = f(\mathbf{x}), \quad \mathbf{x} \in \Gamma_1, \Gamma_2, \Gamma_3, \Gamma_4, \tag{33}$$

$$L_1\Re(u(\mathbf{x})) = (\Delta + \gamma^2)(\Delta - \kappa^2)u(\mathbf{x}) = (\Delta + \gamma^2)f(\mathbf{x}), \quad \mathbf{x} \in \Gamma_1, \Gamma_2, \Gamma_3, \Gamma_4, \tag{34}$$

$$L_2 \ L_1\Re(u(\mathbf{x})) = \Delta(\Delta + \gamma^2)(\Delta - \kappa^2)u(\mathbf{x}) = \Delta(\Delta + \gamma^2)f(\mathbf{x}), \quad \mathbf{x} \in \Gamma_1, \Gamma_2, \Gamma_3, \Gamma_4. \tag{35}$$

Therefore, the discretized system in Equation (20) can be obtained by considering governing Equation (30), the additional boundary conditions described in Equations (30)–(35), and the given boundary conditions with noise data in Equations (29) and (30).

First, different noises controlled by s are considered to obtain the numerical results by using N = 3591, $n_{b1} = n_{b2} = n_{b3} = n_{b4}$ = 57, and n_s = 300. The analytical and numerical solutions in Figure 4 are depicted with black solid and red dashed curves, respectively. Since the noises are given on boundary $\Gamma_1, \Gamma_2, \Gamma_3$, it can be found that the red dashed curves are obviously unstable near these three boundaries in Figure 4, especially when the value of s is large. Meanwhile, the numerical solutions near boundary Γ_4 show the most

unstable results since there is zero information. From the results in Figure 4, we can find that the analytical and numerical solutions are almost identical in Figure 4a when s = 1%. Meanwhile, the deviation of the two curves increases as the value of s enlarges in the other parts of Figure 4. As there is no information on the boundary Γ_4,. the location of the maximum deviation always appears on Γ_4. Therefore, the comparison between analytical and numerical solutions of the boundary nodes on Γ_4 is shown in Figure 5. By observation, the deviation between each numerical and analytical curve will increase when the value of s is enlarging. Additionally, when the value of u is large, a large deviation between the numerical and the analytical curve can be found, especially when s = 5% and s = 7%.

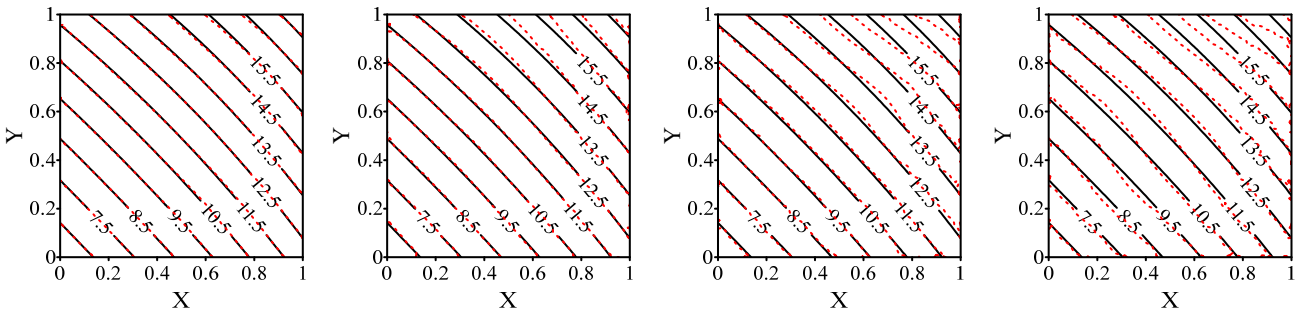

(**a**) s = 1% (**b**) s = 3% (**c**) s = 5% (**d**) s = 7%

Figure 4. The distribution of numerical (dashed curves) and analytical solutions (solid curves).

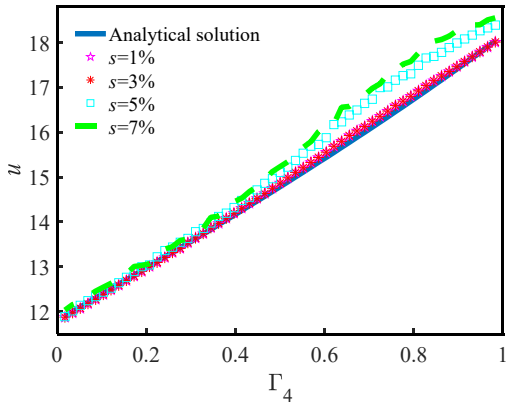

Figure 5. Comparisons between the numerical and analytical solutions on Γ_4.

The numerical tests above show that the LMFS can solve this inhomogeneous inverse Cauchy problem accurately with a group of fixed parameters. Furthermore, in order to test the stability of numerical solutions calculated by the LMFS, the numerical results obtained by using different n_s and N will be discussed. The E_{maxr} and E_{global} are listed in Tables 2 and 3. In Table 2, five different groups of n_s varying from 200 to 360 with fixed N = 3591 are used for the calculation. In Table 3, n_s = 300 is fixed, and N changes from 3591 to 7650. By observing the errors in Tables 2 and 3, it can be found that the values of E_{maxr} are quite close to their corresponding values of s, which can validate the accuracy of the proposed method. In addition, the E_{global} obtained in Tables 2 and 3 also show similar accuracy. In the considered range of the n_s and N, the LMFS shows a strong stability in solving the inhomogeneous inverse Cauchy problem. By using the RC-MRM, although the order of the governing equation is raised, the numerical solutions are still quite accurate.

Table 2. The numerical errors of different number of local nodes.

n_s		200	240	280	320	360
s = 1%	E_{maxr}	1.02×10^{-2}	8.71×10^{-3}	8.46×10^{-3}	9.47×10^{-3}	9.16×10^{-3}
	E_{global}	3.38×10^{-3}	3.62×10^{-3}	3.39×10^{-3}	3.21×10^{-3}	1.69×10^{-3}
s = 3%	E_{maxr}	2.67×10^{-2}	2.64×10^{-2}	2.90×10^{-2}	2.92×10^{-2}	2.84×10^{-2}
	E_{global}	5.81×10^{-3}	7.64×10^{-3}	9.94×10^{-3}	5.80×10^{-3}	6.28×10^{-3}
s = 5%	E_{maxr}	4.95×10^{-2}	4.70×10^{-2}	4.40×10^{-2}	4.77×10^{-2}	4.18×10^{-2}
	E_{global}	2.18×10^{-2}	1.41×10^{-2}	1.76×10^{-2}	8.59×10^{-3}	9.31×10^{-3}
s = 7%	E_{maxr}	6.97×10^{-2}	6.81×10^{-2}	6.45×10^{-2}	6.17×10^{-2}	6.20×10^{-2}
	E_{global}	3.22×10^{-2}	1.71×10^{-2}	1.94×10^{-2}	1.90×10^{-2}	1.08×10^{-2}

During our test, when a fixed N is given, $n_s < 200$ leads to a $E_{maxr} > s$ in Table 2. Meanwhile, the results in Table 3 show that when s = 1%, N changes from 6552 to 7560 with fixed n_s, and E_{maxr} will be close to s. However, the accuracy will be reduced if N is increased. It means that when calculating a high-order governing equation, a large number of n_s should be employed. Here, the order of PDE is the eighth, and more than 200 local nodes are required. In other examples, we discuss whether the accuracy of LMF can be proved by less than 200 local nodes when the order of the governing equation is less than the eighth.

Table 3. The numerical errors of different number of total nodes.

N		3591	4615	5616	6552	7560
s = 1%	E_{maxr}	9.40×10^{-3}	9.64×10^{-3}	9.49×10^{-3}	1.16×10^{-2}	1.47×10^{-2}
	E_{global}	2.29×10^{-3}	2.35×10^{-3}	2.43×10^{-3}	3.63×10^{-3}	5.19×10^{-3}
s = 3%	E_{maxr}	2.64×10^{-2}	2.92×10^{-2}	2.67×10^{-2}	2.83×10^{-2}	3.32×10^{-2}
	E_{global}	6.96×10^{-3}	8.47×10^{-3}	4.35×10^{-3}	1.00×10^{-2}	1.16×10^{-2}
s = 5%	E_{maxr}	4.71×10^{-2}	4.57×10^{-2}	4.64×10^{-2}	4.61×10^{-2}	4.90×10^{-2}
	E_{global}	1.18×10^{-2}	1.78×10^{-2}	1.33×10^{-2}	1.18×10^{-2}	1.17×10^{-2}
s = 7%	E_{maxr}	5.83×10^{-2}	6.03×10^{-2}	6.66×10^{-2}	6.96×10^{-2}	6.77×10^{-2}
	E_{global}	1.70×10^{-2}	1.49×10^{-2}	2.28×10^{-2}	2.34×10^{-2}	3.10×10^{-2}

4.2. Example 2

In this example, an inverse Cauchy problem in a double connected domain is presented. The computational domain consists of two concentric circles, where the inner unit circle locates at a center point $\mathbf{x}$ = [0, 0] and the radius of the outer circle is 1.5, as shown in Figure 6. There is no boundary information on outer boundary Γ_2 in this inverse Cauchy problem. At the same time, the boundary conditions on inner boundary Γ_1 are given with Cauchy noise data.

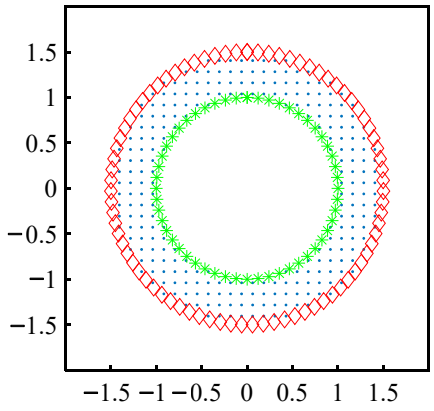

Figure 6. Collocation nodes' distribution.

The original governing equation is given as follows,

$$\Re(u(\mathbf{x})) = (\Delta + \kappa^2)u(\mathbf{x}) = f(\mathbf{x}), \quad \mathbf{x} \in \Omega, \tag{36}$$

where the wavenumber $\kappa = 1$ is given. The inhomogeneous term in Equation (36), the Dirichlet and Neumann boundary conditions on the boundary Γ_1 can be directly obtained from the following analytical solution,

$$u^a(\mathbf{x}) = \sin\left(\frac{\kappa x + \kappa y}{\sqrt{2}}\right) + e^{\gamma x} + e^{\gamma y}, \tag{37}$$

where the constant $\gamma = 1/8\pi$. The noises given in Equations (21) and (22) are considered in the given boundary conditions on boundary Γ_1. By adopting the RC-MRM, a modified Helmholtz operator is used to annihilate the inhomogeneous term, $L_1 f(\mathbf{x}) = (\Delta - \gamma^2) f(\mathbf{x}) = 0$. Thus, the inhomogeneous governing equation can be converted as follows,

$$L_1 \ \Re(u(\mathbf{x})) = (\Delta - \gamma^2)(\Delta + \kappa^2)u(\mathbf{x}) = 0, \quad \mathbf{x} \in \Omega. \tag{38}$$

Since the order of the governing equation is raised by the RC-MRM, the additional boundary conditions are required. The following boundary condition generated from the RC-MRM is used directly without any noise,

$$\Re(u(\mathbf{x})) = (\Delta + \kappa^2)u(\mathbf{x}) = f(\mathbf{x}), \quad \mathbf{x} \in \Gamma_1, \Gamma_2. \tag{39}$$

Firstly, $N = 3259$, and $n_s = 120$ is used to test this inverse Cauchy problem. In Figure 7, the black solid contours represent the analytical solution, and the red dashed contours represent the numerical solution. Since the noises are given on boundary Γ_1, the red dashed curves are unstable near the outer boundary in Figure 7, especially when the value of s is large. When $s = 1\%$, the numerical and analytical solutions are almost close to each other in Figure 7a. When s increases to 3%, 5%, and 7%, the deviation between the numerical and analytical solutions keeps increasing. Meanwhile, due to the missing boundary conditions of boundary Γ_2, the maximum deviation always appears on the outer boundary. Therefore, the details of numerical and analytical solutions on the boundary Γ_2 are shown in Figure 8, where θ is the angular coordinate of the outer boundary node in the polar coordinate system. From the Figure 8, we can see that the deviation between numerical and analytical curve increases when the value of s is enlarging, and a large deviation can always be found when the value of u is large.

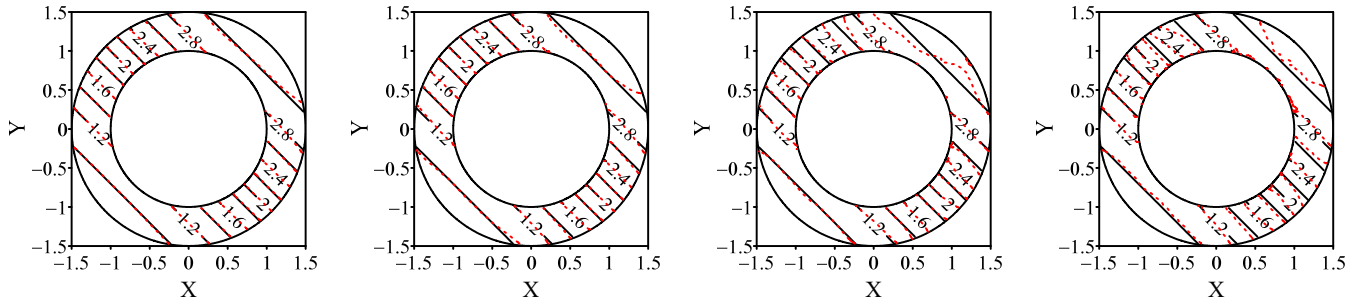

(**a**) $s = 1\%$ (**b**) $s = 3\%$ (**c**) $s = 5\%$ (**d**) $s = 7\%$

Figure 7. The comparison of numerical (dashed curves) and analytical solutions (solid curves).

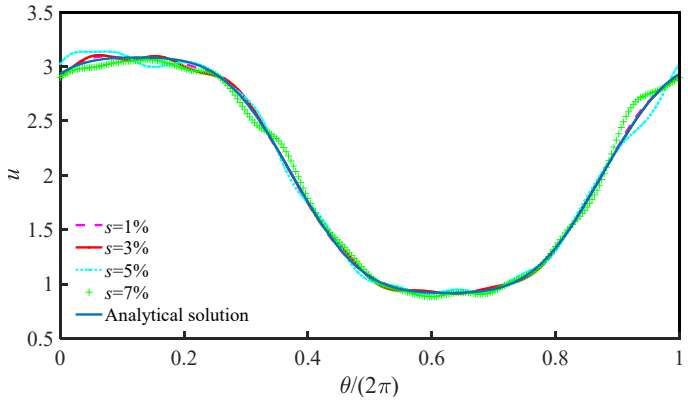

Figure 8. Comparisons between the numerical and analytical solutions on Γ_2.

Then, the stability of the LMFS with different parameters is discussed. In order to test the influence of n_s, we selected five groups of local nodes with fixed $N = 3259$ to evaluate the numerical errors in Table 4. The accuracy of the numerical results can be validated by the comparing the values of E_{maxr} and the given noises s. In Table 4, the values of the E_{maxr} and s are very close to each other. Meanwhile, the values of E_{global} listed in the Table 4 are generally smaller. When N remains unchanged and n_s increases, a larger n_s makes the numerical errors smaller. However, more local nodes lead the system matrix to a full matrix, which increases the computational costs. Giving consideration to the accuracy and efficiency, $n_s = 120$ is suggested in this example.

In the last part of this example, the influence of N is tested by using five different N with fixed $n_s = 120$. The values of E_{maxr} are approximate to the values of given noises, and the values of E_{global} are quite small in Table 5. Numerical results validate that the LMFS can be applied to a big range of N. In addition, when the n_s is fixed, the increase of N will lead to a slight increase of errors. Then, the E_{maxr} are not close to the value of given noise data, especially when N is too large. These results show that there is an upper limit on the selection of N with a fixed n_s. Similar with the results obtained in Example 1, when a larger N is used, more local nodes should be used to guarantee the accuracy. Furthermore, although the order of the original governing equation is raised by the RC-MRM, the LMFS can still obtain very accurate numerical results by using 120 local nodes even when $N = 8834$. Compared with Example 1, less local nodes are required since the order of the governing equation is only the fourth.

Table 4. The numerical errors with different number of local nodes.

n_s		80	100	120	140	160
$s = 1\%$	E_{maxr}	1.32×10^{-2}	1.18×10^{-2}	1.05×10^{-2}	9.84×10^{-3}	8.30×10^{-3}
	E_{global}	3.66×10^{-3}	3.02×10^{-3}	3.51×10^{-3}	2.56×10^{-3}	2.27×10^{-3}
$s = 3\%$	E_{maxr}	3.02×10^{-2}	3.15×10^{-2}	3.07×10^{-2}	3.00×10^{-2}	2.84×10^{-2}
	E_{global}	9.41×10^{-3}	7.09×10^{-3}	6.50×10^{-3}	6.66×10^{-3}	7.44×10^{-3}
$s = 5\%$	E_{maxr}	5.21×10^{-2}	5.13×10^{-2}	5.20×10^{-2}	4.98×10^{-2}	4.66×10^{-2}
	E_{global}	1.73×10^{-2}	1.51×10^{-2}	1.54×10^{-2}	1.81×10^{-2}	1.38×10^{-2}
$s = 7\%$	E_{maxr}	7.84×10^{-2}	7.25×10^{-2}	7.19×10^{-2}	6.78×10^{-2}	6.90×10^{-2}
	E_{global}	2.26×10^{-2}	1.77×10^{-2}	1.87×10^{-2}	2.12×10^{-2}	1.69×10^{-2}

The LMFS shows its stability and effectiveness of in a double connected computational domain in this example. Since the traditional MFS can hardly be applied in complex geometrics of the inverse problem, in the next example, we further study an inverse problem composed of a multi-connected domain.

Table 5. The numerical errors with different number of total nodes.

N		3259	4661	6052	7405	8834
$s = 1\%$	E_{maxr}	1.05×10^{-2}	1.10×10^{-2}	1.10×10^{-2}	1.19×10^{-2}	1.41×10^{-2}
	E_{global}	3.15×10^{-3}	3.01×10^{-3}	3.00×10^{-3}	3.67×10^{-3}	3.54×10^{-3}
$s = 3\%$	E_{maxr}	3.07×10^{-2}	2.99×10^{-2}	3.38×10^{-2}	3.47×10^{-2}	3.78×10^{-2}
	E_{global}	6.50×10^{-3}	9.48×10^{-3}	1.01×10^{-2}	1.01×10^{-2}	1.28×10^{-2}
$s = 5\%$	E_{maxr}	5.20×10^{-2}	5.22×10^{-2}	5.26×10^{-2}	5.49×10^{-2}	5.57×10^{-2}
	E_{global}	1.54×10^{-2}	1.50×10^{-2}	1.44×10^{-2}	1.69×10^{-2}	1.72×10^{-2}
$s = 7\%$	E_{maxr}	7.19×10^{-2}	7.00×10^{-2}	7.19×10^{-2}	8.35×10^{-2}	8.38×10^{-2}
	E_{global}	1.87×10^{-2}	2.17×10^{-2}	1.64×10^{-2}	2.25×10^{-2}	2.88×10^{-2}

4.3. Example 3

This example introduces another inhomogeneous problem in an irregular multi-connected domain, as shown in Figure 9. For some engineering problems, the boundaries of hidden holes are irregular, and their boundary conditions can be hardly measured. The multi-connected domain Ω, which is the same as what was used in [32], is composed of a symmetrical outer boundary Γ_1 and three irregular inner boundaries Γ_2, Γ_3, and Γ_4. The parametric equations of the irregular boundaries can be defined as follows,

$$\Gamma_t = \{(x,y)|x = \rho_t(\theta)\cos(\theta) + c_t, y = \rho_t(\theta)\sin(\theta), 0 \le \theta \le 2\pi\},\ t = 1,2,3,4, \tag{40}$$

where θ represents the angles in polar coordinates of the boundary nodes along each boundary, $c_1 = c_2 = 0, c_3 = -3, c_4 = 3, \rho_1(\theta) = 4\sqrt{\cos 2\theta + \sqrt{1.1 - \sin^2 2\theta}}, \rho_2(\theta) = 0.5(\cos 3\theta + \sqrt{2 - \sin^2 3\theta})^{1/3}, \rho_3(\theta) = 0.5 + \cos^2 4\theta$, and $\rho_4(\theta) = 0.7\left(e^{\sin\theta}\sin^2 2\theta + e^{\cos\theta}\cos^2 2\theta\right)$. The original governing equation can be written as,

$$\Re(u(\mathbf{x})) = \Delta u(\mathbf{x}) = f(\mathbf{x}), \quad \mathbf{x} \in \Omega. \tag{41}$$

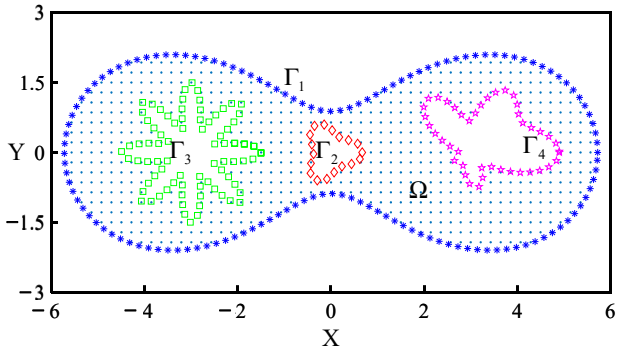

Figure 9. Collocation nodes' distribution.

Unlike the boundary conditions in Example 2, the Cauchy data are used in the outer boundary Γ_1, while no information is employed on Γ_2, Γ_3, and Γ_4. Similar to the work in [32], the Cauchy problem with missing boundary conditions of the inner boundaries is solved. However, the numerical problem in this example is inhomogeneous, which means it cannot be solved directly by the LMFS. For the inhomogeneous term in Equation (41), the Dirichlet and Neumann boundary conditions can be obtained by the analytical solution as follows,

$$u^a(\mathbf{x}) = \sin(\gamma x) + \sin(\gamma y) + \frac{1}{6}\left(\left(\frac{x}{2}\right)^3 + \left(\frac{y}{2}\right)^3\right) + 10, \tag{42}$$

where the constant $\gamma = 3/4$ is used. The noise data in Equations (21) and (22) are imposed on the Dirichlet and Neumann boundary conditions on the boundary Γ_1. By adopting the RC-MRM, a Helmholtz operator and a Laplace operator are used to annihilate the inho-

mogeneous term for Equation (41), which can be shown as $L_2L_1f(\mathbf{x}) = \Delta(\Delta + \gamma^2)f(\mathbf{x}) = 0$. Therefore, a new homogeneous governing equation can be formed as follows,

$$L_2L_1 \ \Re(u(\mathbf{x})) = \Delta(\Delta + \gamma^2)\Delta u(\mathbf{x}) = 0, \quad \mathbf{x} \in \Omega. \tag{43}$$

The order of the original governing equation is increased by the RC-MRM, and the new homogeneous governing equation is transformed into a sixth-order PDE. Then, two additional boundary conditions without considering any additional noises are imposed on the whole boundaries as follows,

$$\Re(u(\mathbf{x})) = \Delta u(\mathbf{x}) = f(\mathbf{x}), \quad \mathbf{x} \in \Gamma_1, \Gamma_2, \Gamma_3, \Gamma_4, \tag{44}$$

$$L_1 \ \Re(u(\mathbf{x})) = (\Delta + \gamma^2)\Delta u(\mathbf{x}) = (\Delta + \gamma^2)f(\mathbf{x}), \quad \mathbf{x} \in \Gamma_1, \Gamma_2, \Gamma_3, \Gamma_4. \tag{45}$$

Firstly, $N = 3144$ and $n_s = 120$ are used to test this problem. The analytical and numerical solutions are depicted by black solid contours and red dashed contours, respectively, in Figure 10. From the Figure 10, we can see that when $s = 1\%$, the contours of numerical solution and analytical solution fit well. As the value of s increases, the deviation between the two kinds of contours is becoming larger. Although some unstable results appear on the outer boundary, the most unstable numerical results are located on the inner boundaries, where zero boundary information can be obtained. This phenomenon is similar with the previous examples. Therefore, in order to further show the detailed numerical results of each inner boundary, the numerical and analytical solutions on boundaries Γ_2, Γ_3, and Γ_4 are presented in Figures 11–13. In Figures 11–13, when $s = 1\%$ the analytical and numerical solutions all are almost consistent with each other on the inner boundaries, the largest absolute deviation can be found on boundary Γ_4. From the details in the last part of Figure 13, when $s = 7\%$, the maximum relative error E_{maxr} is close to 6.67%. However, the maximum relative error on the inner boundary is still close to its given noise data, which validates the efficiency of the proposed LMFS.

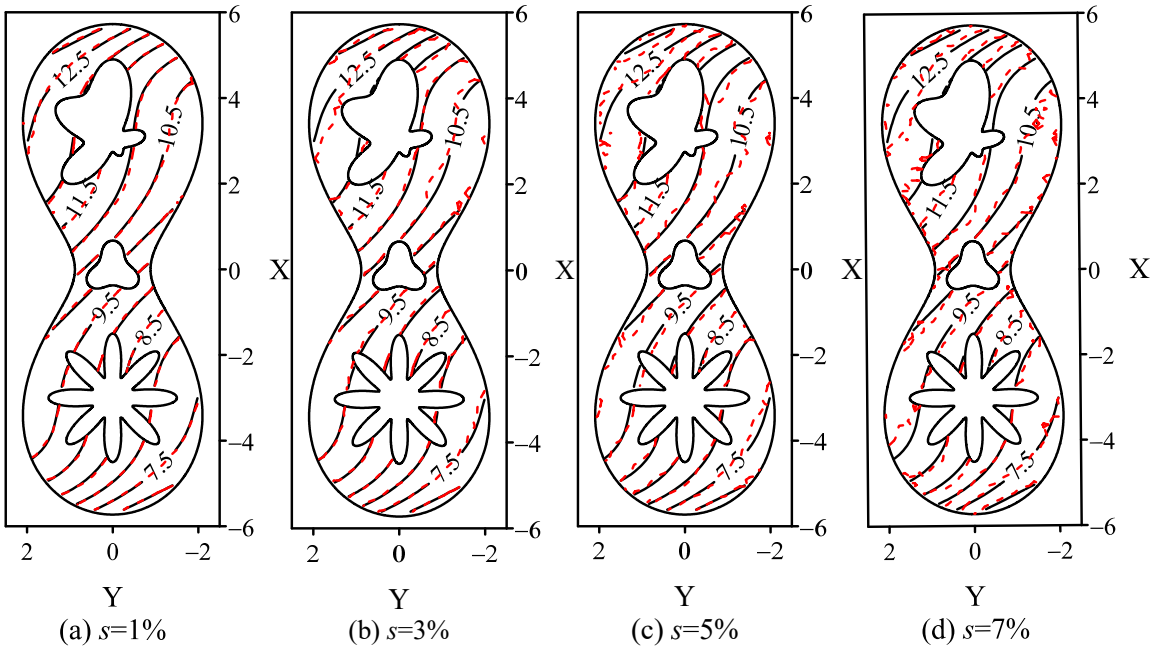

Figure 10. The comparison of numerical (dashed curves) and analytical solutions (solid curves).

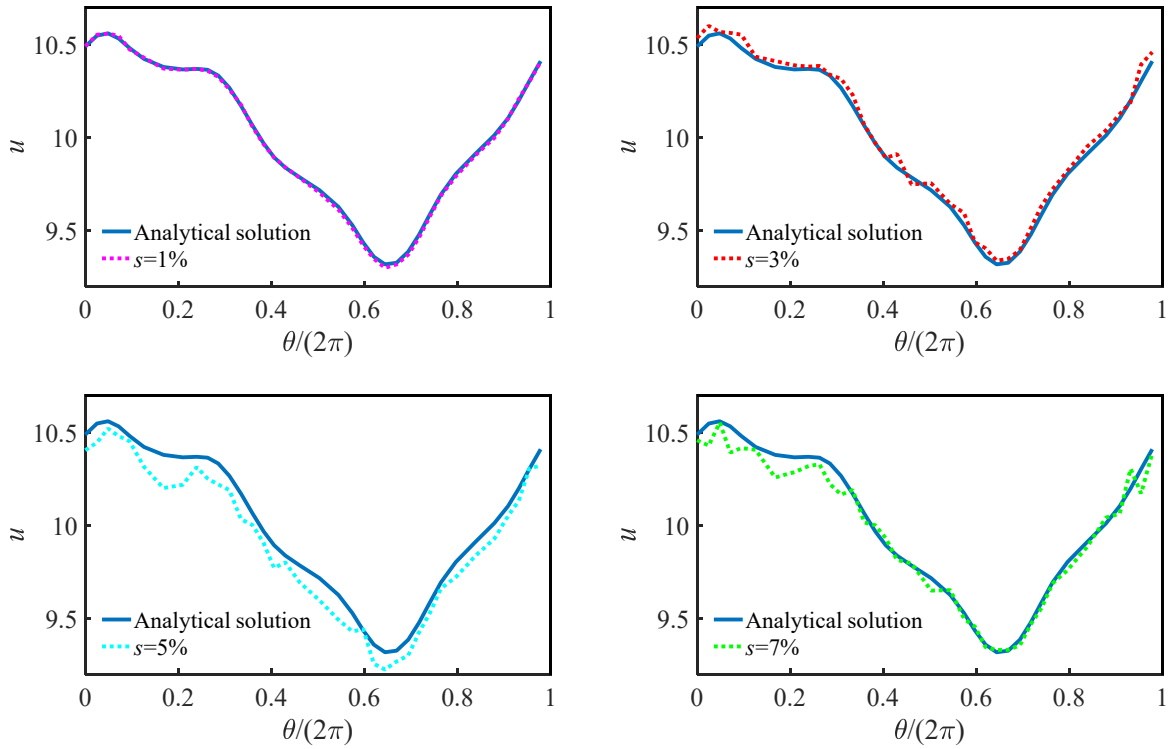

Figure 11. Comparisons between the numerical and analytical solutions on boundary Γ_2.

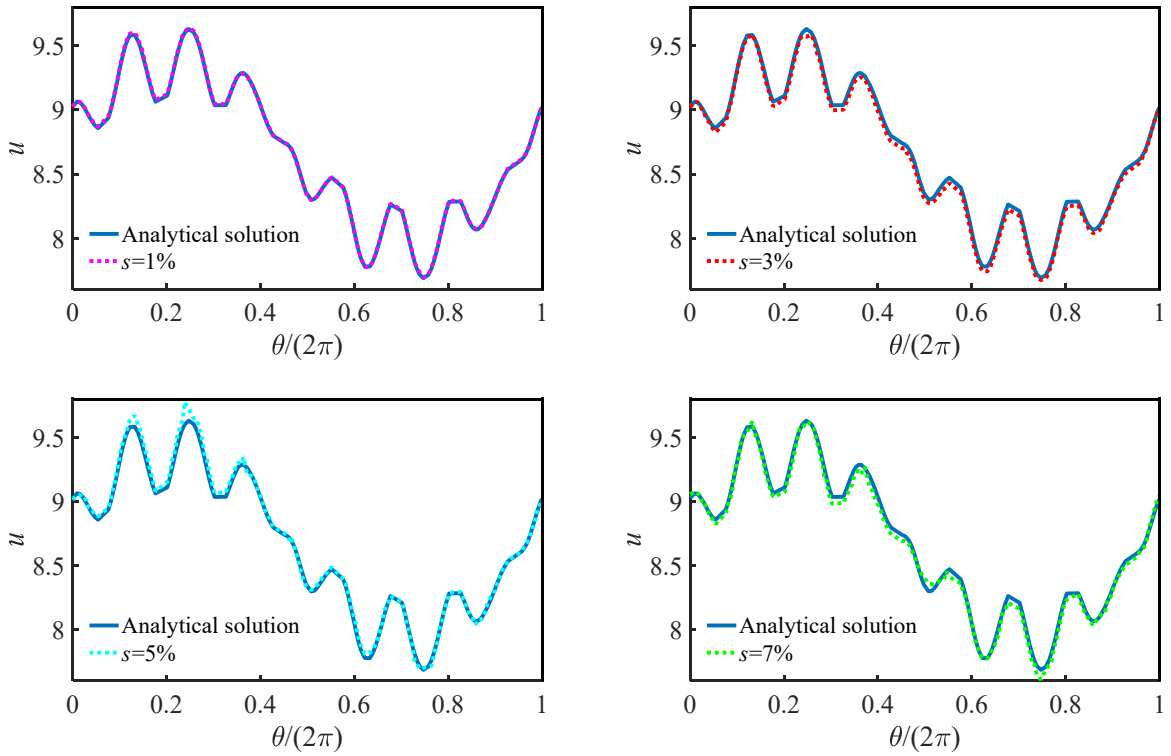

Figure 12. Comparisons between the numerical and analytical solutions on boundary Γ_3.

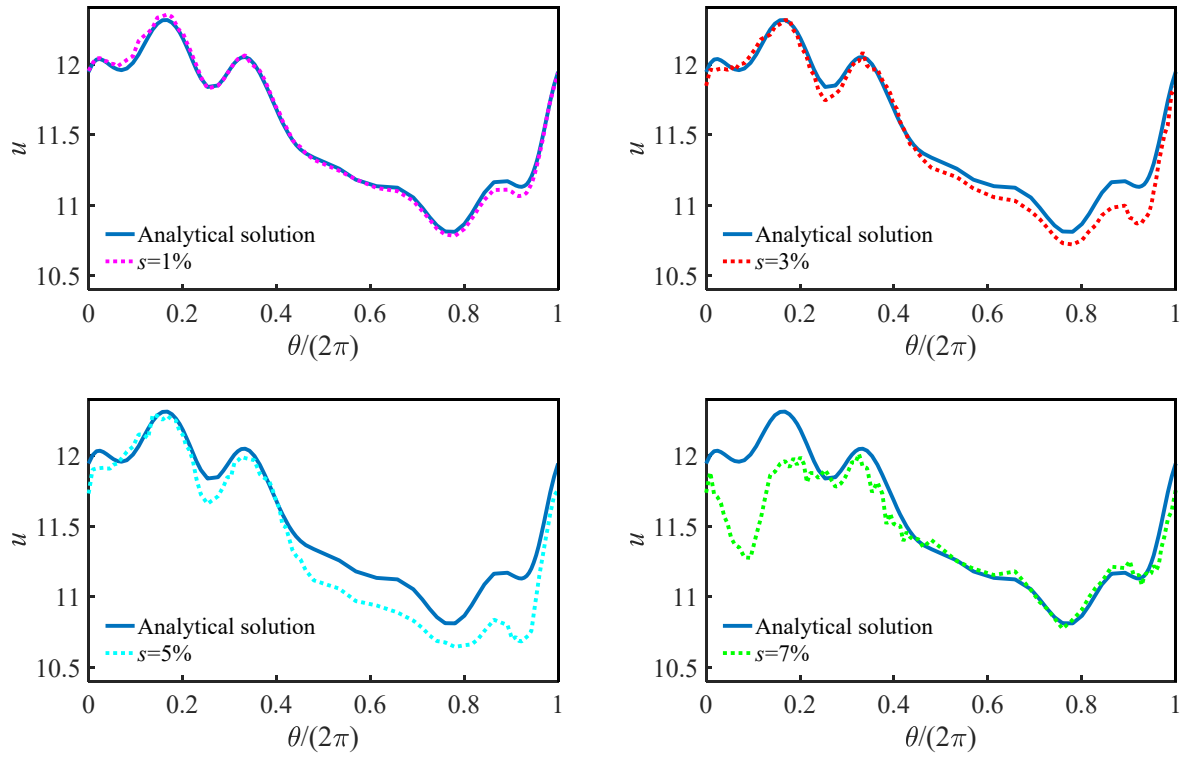

Figure 13. Comparisons between the numerical and analytical solutions on boundary Γ_4.

The convergence rate of the LMFS is presented in Tables 6 and 7. In Table 6, different n_s are tested with fixed N = 3144. When n_s ranges from 100 to 200, the values of E_{maxr} and s are almost identical. Meanwhile, E_{global} is stable in the range of [0.001, 0.01]. These results show that, when $n_s \geq 100$ and N = 3144, the numerical results calculated by the LMFS are accurate. Then, considering the homogeneous governing equation is a sixth-order PDE, n_s = 180 is used to test the influence of N in the Table 7.

Table 6. The numerical errors with different number of local nodes.

n_s		100	120	160	180	200
s = 1%	E_{maxr}	9.62×10^{-3}	8.05×10^{-3}	9.04×10^{-3}	9.95×10^{-3}	9.70×10^{-3}
	E_{global}	2.58×10^{-3}	2.16×10^{-3}	2.02×10^{-3}	2.22×10^{-3}	1.99×10^{-3}
s = 3%	E_{maxr}	2.82×10^{-2}	2.37×10^{-2}	2.90×10^{-2}	2.82×10^{-2}	2.83×10^{-2}
	E_{global}	7.49×10^{-3}	6.16×10^{-3}	5.56×10^{-3}	6.32×10^{-3}	5.89×10^{-3}
s = 5%	E_{maxr}	4.38×10^{-2}	4.08×10^{-2}	4.59×10^{-2}	4.73×10^{-2}	4.88×10^{-2}
	E_{global}	1.35×10^{-2}	1.09×10^{-2}	1.08×10^{-2}	1.00×10^{-2}	1.12×10^{-2}
s = 7%	E_{maxr}	6.98×10^{-2}	6.11×10^{-2}	6.17×10^{-2}	6.32×10^{-2}	5.85×10^{-2}
	E_{global}	1.74×10^{-2}	1.59×10^{-2}	1.43×10^{-2}	1.24×10^{-2}	1.28×10^{-2}

Table 7. The numerical errors with different number of local nodes.

N		1629	3472	4562	6047	7680
s = 1%	E_{maxr}	9.95×10^{-3}	9.75×10^{-3}	8.09×10^{-3}	9.27×10^{-3}	1.16×10^{-2}
	E_{global}	1.96×10^{-3}	2.40×10^{-3}	1.59×10^{-3}	2.08×10^{-3}	2.14×10^{-3}
s = 3%	E_{maxr}	2.60×10^{-2}	2.80×10^{-2}	2.67×10^{-2}	2.67×10^{-2}	2.88×10^{-2}
	E_{global}	5.40×10^{-3}	6.71×10^{-3}	5.66×10^{-3}	5.95×10^{-3}	6.99×10^{-3}
s = 5%	E_{maxr}	4.92×10^{-2}	4.99×10^{-2}	4.26×10^{-2}	4.00×10^{-2}	4.71×10^{-2}
	E_{global}	8.94×10^{-3}	1.04×10^{-2}	8.82×10^{-3}	7.97×10^{-3}	8.75×10^{-3}
s = 7%	E_{maxr}	6.91×10^{-2}	6.72×10^{-2}	5.73×10^{-2}	6.89×10^{-2}	6.46×10^{-2}
	E_{global}	1.39×10^{-2}	1.61×10^{-2}	1.32×10^{-2}	1.24×10^{-2}	1.34×10^{-2}

As shown in Table 7, the value of E_{maxr} is slightly smaller or close to s, except when $s = 1\%$ and $N = 7680$, E_{maxr} =1.17%≈s. All the numerical errors show good accuracy of the LMFS. The values of E_{global} in Table 7 are all quite small and similar with those in Table 6. When the value of N is larger than 7860, more local nodes are needed to guarantee the accuracy. According to Equation (43), as the order of the final governing equation in this example is lower than that in Example 1, and higher than that in Example 2, the value of n_s used in this example is smaller than Example 1 and larger than Example 2 when considering the same N. This can be validated by the numerical results calculated with $N = 7560$ in Table 3, $N = 7405$ in Table 5, and $N = 7680$ in Table 7. The results show that more local nodes are suggested for calculating when the order of the final governing equation is higher.

4.4. Example 4

In this part, an inhomogeneous inverse problem without an analytical solution is proposed. The mixed Dirichlet and Neumann boundary conditions are given in this problem. It should be emphasized that, in order to simulate the engineering problems, the two kinds of boundary conditions can neither be derived from each other nor meet the governing equations. The inverse Cauchy problem was proposed recently by Fan et al. [33], which can be introduced as two steps: the direct problem and inverse problem. Then, the details of the irregular boundary are shown in Figure 14, where θ represents the angles of polar coordinates of the boundary nodes. The formulas of the boundaries are presented as follows,

$$\begin{cases} \Gamma_1 = \left\{(x,y) \middle| x = \rho(\theta)\cos\theta, y = \rho(\theta)\sin\theta, 0 \le \theta < \frac{3}{2}\pi\right\}, \ \rho(\theta) = 1 + \cos^2 4\theta, \\ \Gamma_2 = \left\{(x,y) \middle| x = \rho(\theta)\cos\theta, y = \rho(\theta)\sin\theta, \frac{3}{2}\pi \le \theta < 2\pi\right\}, \ \rho(\theta) = 1 + \cos^2 4\theta, \end{cases} \tag{46}$$

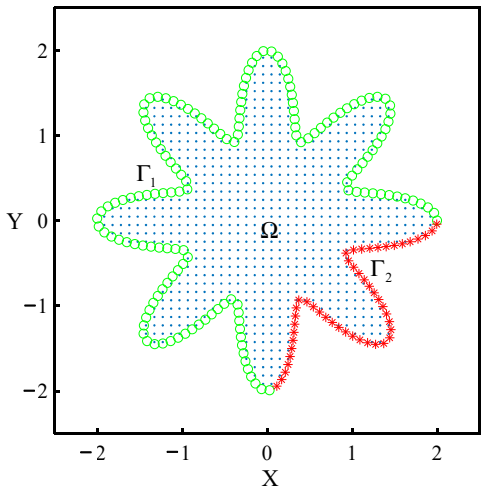

Figure 14. Collocation nodes' distribution.

Step 1. Direct problem:

The direct problem introduces a Poisson equation as the governing equation. In addition, the Neumann boundary condition is given on the boundary Γ_1 and the Dirichlet boundary condition is given on the boundary Γ_2. The governing equation and the boundary conditions are given as follows:

$$\Re(u(\mathbf{x})) = \Delta u(\mathbf{x}) = f(\mathbf{x}) = \frac{3}{2}(x + y), \ \mathbf{x} \in \Omega, \tag{47}$$

$$\frac{\partial u(\mathbf{x})}{\partial \mathbf{n}} = \frac{4}{5}(x + y), \ \mathbf{x} \in \Gamma_1, \tag{48}$$

$$u(\mathbf{x}) = \left(\sinh\left(\frac{x}{\pi}\right) + \cosh\left(\frac{x}{\pi}\right)\right)\sin\left(\frac{y}{4}\right) + x + y + 40,\ \mathbf{x} \in \Gamma_2. \tag{49}$$

Meanwhile, through the using of RC-MRM, the inhomogeneous governing equation can be transformed into the following homogeneous form,

$$L_1\Re(u(\mathbf{x})) = \Delta\Delta u(\mathbf{x}) = \Delta f(\mathbf{x}) = 0,\ \mathbf{x} \in \Omega. \tag{50}$$

Therefore, the Poisson equation is changed into a biharmonic equation, which can be solved by the LMFS directly. Since the order of differential operator is increased, the additional boundary condition on the whole boundary is given as follows,

$$\Re(u(\mathbf{x})) = \Delta u(\mathbf{x}) = f(\mathbf{x}) = \frac{3}{2}(x+y),\ \mathbf{x} \in \Gamma_1, \Gamma_2. \tag{51}$$

Then, the LMFS can solve the direct problem governed by the new governing equation, Equation (50), with the given boundary conditions and the additional boundary condition (Equation (51)) directly. Since no analytical solution can be used for comparison, it is hard to verify the accuracy of numerical results. Thus, an inverse Cauchy problem is introduced in Step 2 for solving this problem. It should be emphasized that the LMFS is still applied to this inverse Cauchy problem. In addition, the boundary data Γ_2 in Step 1 denoted as u_2 are used as the given information in Step 2.

Step 2. Inverse problem:

By using the LMFS with RCMRM in Step 1, we have the numerical solutions $\hat{u}$ of all the collocation nodes. In Step 2, we note the value of $\hat{u}$ on boundary Γ_1 as $\hat{u}_1$. Thus, the new defined $\hat{u}_1$ can be used as the Dirichlet boundary condition on boundary Γ_1 in Step 2. The above description can be summarized as the following formula,

$$u(\mathbf{x}) = \hat{u}_1,\ \mathbf{x} \in \Gamma_1. \tag{52}$$

Then, we remove the original boundary condition on boundary Γ_2 and regard it as a boundary with no information. Thus, the original governing Equation (47), the given Neumann boundary condition (48), and the new Dirichlet boundary condition (52) on boundary Γ_1, consist of a new inhomogeneous inverse Cauchy problem. Similarly, the RC-MRM can be used to transform the governing equation from Equation (47) into a homogeneous Equation (50). Moreover, the additional boundary condition (51) can help the LMFS to solve this inverse Cauchy problem directly. Unlike the previous examples, we do not put any noise on boundary conditions in this example. Because the numerical solutions from Step 1 contain numerical errors, there is no need to add extra noise into the boundary conditions. The final numerical solution is denoted as $\overline{u}$ in Step 2.

The comparison of the contours of $\hat{u}$ and $\overline{u}$ calculated by different N and n_s can be seen in Figures 15 and 16, respectively. In order to test the influence of N, $n_s = 100$ is used to obtain numerical results in Figure 15. Since the final governing equation is a second-order PDE, the value of n_s is suggested to be located in between 40 and 100, and the influence of the local nodes is tested in Figure 16. The contour maps show that no matter how many total nodes or local nodes are used, the numerical solutions between the direct problem and the inverse problem are close to each other. Since no noise is added, the contours of the direct problem and the inverse problem can be completely well fit with each other on boundary Γ_1, while the deviation between the contours only occurs far away from this boundary. It is easy to find that almost all the maximum deviations occur near boundary Γ_2, especially in the middle of this boundary. In order to further show the accuracy of the LMFS, we compare the numerical solutions on boundary Γ_2 to find out the specific value of the deviation in Figures 17 and 18.

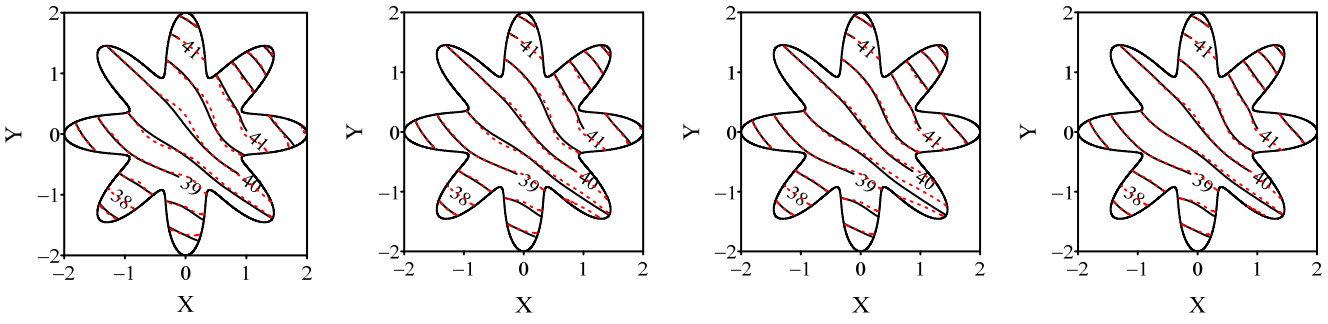

(**a**) $N = 3585$ (**b**) $N = 5500$ (**c**) $N = 7561$ (**d**) $N = 9505$

Figure 15. The comparison of numerical solutions of direct problem (solid curve) and inverse problem (dashed curve).

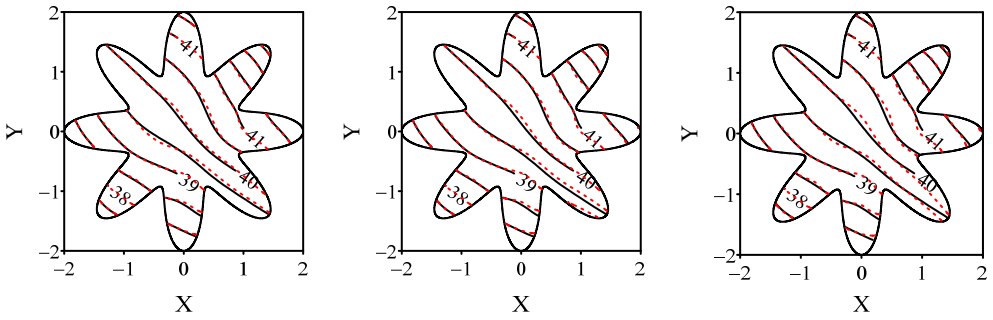

(**a**) $n_s = 40$ (**b**) $n_s = 60$ (**c**) $n_s = 80$

Figure 16. The comparison of numerical solutions of direct problem (solid curve) and inverse problem (dashed curve).

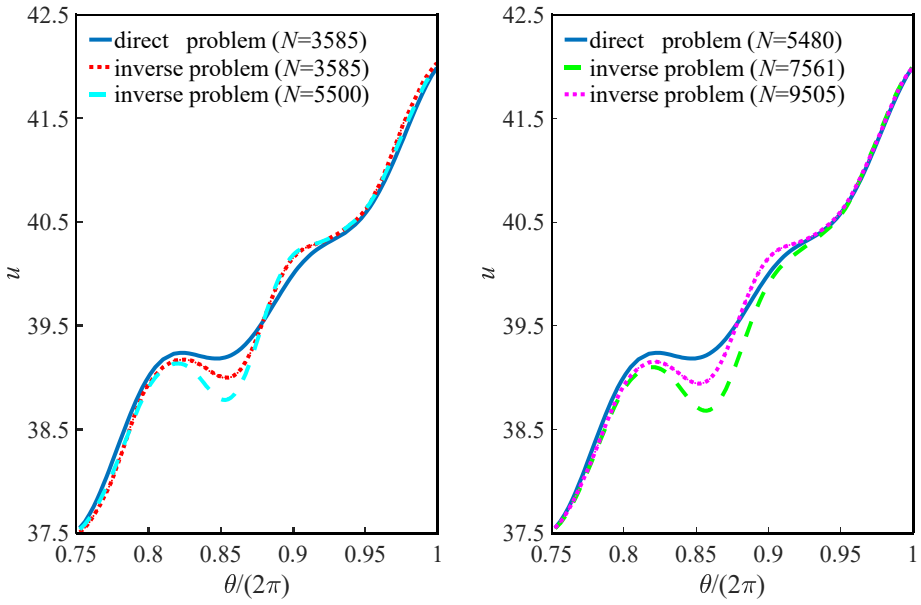

Figure 17. Comparison between $\overline{u}_2$ in Step 2 (dashed lines) and u_2 in Step 1 (solid line) on Γ_2.

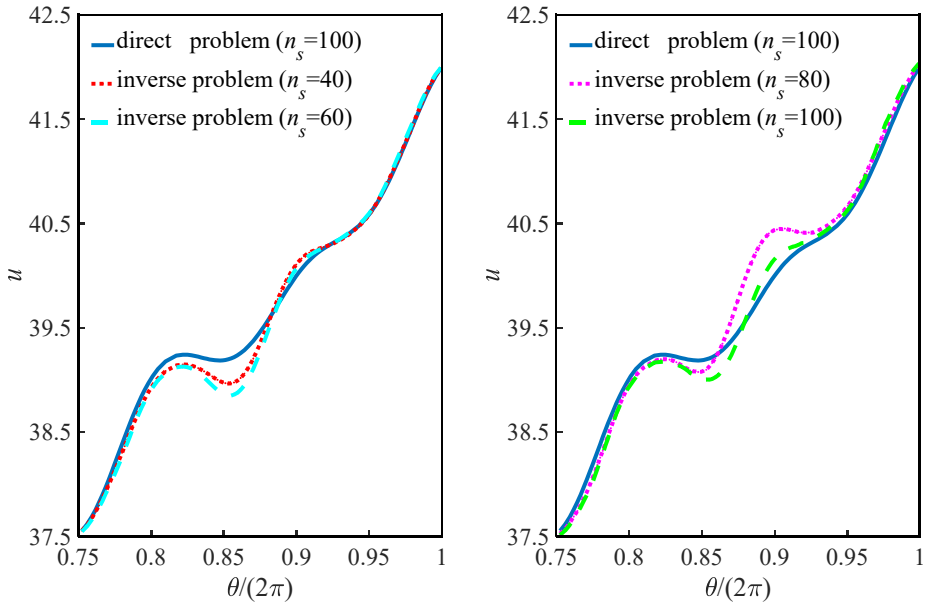

Figure 18. Comparison between $\overline{u}_2$ in Step 2 (dashed lines) and u_2 in Step 1 (solid line) on Γ_2.

The numerical solution on boundary Γ_2 in Step 2 is defined as $\overline{u}_2$. Figures 17 and 18 show the details of the numerical results from Figures 15 and 16 on Γ_2, respectively. The numerical curves of u_2 and $\overline{u}_2$ can are compared in detail, where the curves in Figures 17 and 18 fit well with each other, and only small deviations can be found between every two curves. The maximum deviation always appears in the middle of the curves, which draws the same conclusions as Figures 15 and 16. These numerical results show that the most inaccurate position often appears at the position that is far away from the boundary with the given boundary conditions. Meanwhile, the maximum deviation appears on the curve when $N = 7561$ in Figure 17, where $u_2 \approx 39$, and the maximum deviation can be found as less than 1. Then, the relative deviation is approximated to $1/39 < 3\%$, which is smaller than the allowable error in many engineering problems.

5. Conclusions

In this paper, the LMFS is firstly used for solving the inverse Cauchy problems of two-dimensional inhomogeneous problems based on the RC-MRM without considering any particular solutions. Four numerical examples with and without analytical solutions are provided in this paper. Different noise data are considered in our numerical examples. From the presented numerical results and analysis, it is clear that the proposed LMFS can solve the inverse Cauchy problem of different geometries accurately and stably. The number of the local nodes is related to the order of the formulated PDE in the RC-MRM. The numerical errors are convergent to the same level of the given noise data as the number of nodes increases. Some useful suggestions and experience are presented in detail for the LMFS in solving the inverse Cauchy problem.

Author Contributions: Formal analysis, J.Z., H.Z. and C.-M.F. and M.-F.F. All authors have read and agreed to the published version of the manuscript.

Funding: This work is supported by the National Natural Science Foundation of China (No: 12172159), National Natural Science Foundation of Jiangxi Provence (No: 20212BAB211022). The authors are very thankful for Jiangxi double thousand talents support (No: jxsq2018106027).

Conflicts of Interest: The authors declare no conflict of interest.

References

1. Chakib, A.; Nachaoui, A. Convergence analysis for finite element approximation to an inverse Cauchy problem. *Inverse Probl.* **2006**, *22*, 1191–1206. [CrossRef]
2. Vanrumste, B.; Van Hoey, G.; Van de Walle, R.; Michel, R.D.; Lemahieu, I.A.; Boon, P.A. The validation of the finite difference method and reciprocity for solving the inverse problem in EEG dipole source analysis. *Brain Topogr.* **2001**, *14*, 83–92. [CrossRef] [PubMed]
3. Lesnic, D.; Elliott, L.; Ingham, D.B. An alternating boundary element method for solving Cauchy problems for the biharmonic equation. *Inverse Probl. Eng.* **1997**, *5*, 145–168. [CrossRef]
4. Marin, L.; Elliott, L.; Ingham, D.B.; Lesnic, D. Boundary element method for the Cauchy problem in linear elasticity. *Eng. Anal. Bound. Elem.* **2001**, *25*, 783–793. [CrossRef]
5. Marin, L.; Hao, D.N.; Lesnic, D. Conjugate gradient-boundary element method for a Cauchy problem in the Lame system. In *BETECH XIV*; Brebbia, C.A., Kassab, A.J., Eds.; WTT Press: Southampton, UK, 2001; pp. 229–238.
6. Liu, C.S. A modified collocation Trefftz method for the inverse Cauchy problem of Laplace equation. *Eng. Anal. Bound. Elem.* **2008**, *32*, 778–785. [CrossRef]
7. Liu, C.S.; Atluri, S.N. Numerical solution of the Laplacian Cauchy problem by using a better postconditioning collocation Trefftz method. *Eng. Anal. Bound. Elem.* **2013**, *37*, 74–83. [CrossRef]
8. Yang, J.P.; Hsin, W.C. Weighted reproducing kernel collocation method based on error analysis for solving inverse elasticity problems. *Acta Mech.* **2019**, *230*, 3477–3497. [CrossRef]
9. Zhang, T.; Dong, L.T.; Alotaibi, A.; Atluri, S.N. Application of the MLPG mixed collocation method for solving inverse problems of linear isotropic/anisotropic elasticity with simply/multiply-connected domains. *CMES Comput. Model. Eng. Sci.* **2013**, *94*, 1–28.
10. Zheng, H.; Zhang, C.; Wang, Y.S.; Chen, W.; Sladek, J.; Sladek, V. A local RBF collocation method for band structure computations of 2D solid/fluid and fluid/solid phononic crystals. *Int. J. Numer. Methods Eng.* **2017**, *110*, 467–500. [CrossRef]
11. Zheng, H.; Zhang, C.; Wang, Y.S.; Sladek, J.; Sladek, V. A meshfree local RBF collocation method for anti-plane transverse elastic wave propagation analysis in 2D phononic crystals. *J. Comput. Phys.* **2016**, *305*, 997–1014. [CrossRef]
12. Cheng, H.D.; Hong, Y.X. An overview of the method of fundamental solutions—Solvability, uniqueness, convergence, and stability. *Eng. Anal. Bound. Elem.* **2020**, *120*, 118–152. [CrossRef]
13. Jin, B.T.; Zheng, Y. Boundary knot method for the Cauchy problem associated with the inhomogeneous Helmholtz equation. *Eng. Anal. Bound. Elem.* **2005**, *29*, 925–935. [CrossRef]
14. Gu, Y.; Chen, W.; Fu, Z.J. Singular boundary method for inverse heat conduction problems in general anisotropic media. *Inverse Probl. Sci. Eng.* **2014**, *129*, 124–136. [CrossRef]
15. Chen, W.; Fu, Z.J. Boundary particle method for inverse Cauchy problems of inhomogeneous Helmholtz equations. *J. Mar. Sci. Technol.* **2009**, *17*, 157–163. [CrossRef]
16. Karageorghis, A.; Fairweather, G. The method of fundamental solutions for the numerical solution of the biharmonic equation. *J. Comput. Phys.* **1987**, *69*, 433–459. [CrossRef]
17. Karageorghis, A.; Lesnic, D.; Marin, L. A survey of applications of the MFS to inverse problems. *Inverse Probl. Sci. Eng.* **2011**, *19*, 309–336. [CrossRef]
18. Rek, Z.; Sarler, B. The method of fundamental solutions for the Stokes flow with the subdomain technique. *Eng. Anal. Bound. Elem.* **2021**, *128*, 80–89. [CrossRef]
19. Flyer, N.; Fornberg, B.; Bayona, V.; Barnett, G.A. On the role of polynomials in RBF-FD approximations: I. Interpolation and accuracy. *J. Comput. Phys.* **2016**, *321*, 21–38. [CrossRef]
20. Bayona, V.; Flyer, N.; Fornberg, B.; Barnett, G.A. On the role of polynomials in RBF-FD approximations: II. Numerical solution of elliptic PDEs. *J. Comput. Phys.* **2017**, *332*, 257–273. [CrossRef]
21. Fan, C.M.; Huang, Y.K.; Chen, C.S.; Kuo, S.R. Localized method of fundamental solutions for solving two-dimensional Laplace and biharmonic equations. *Eng. Anal. Bound. Elem.* **2019**, *101*, 188–197. [CrossRef]
22. Qu, W.Z.; Fan, C.M.; Gu, Y.; Wang, F.J. Analysis of three-dimensional interior acoustic fields by using the localized method of fundamental solutions. *Appl. Math.* **2019**, *76*, 122–132. [CrossRef]
23. Gu, Y.; Fan, C.M.; Qu, W.Z.; Wang, F.J. Localized method of fundamental solutions for large-scale modelling of three-dimensional anisotropic heat conduction problems. *Comput. Struct.* **2019**, *220*, 144–155. [CrossRef]
24. Nowak, A.J.; Partridge, P.W. Comparison of the dual reciprocity and the multiple reciprocity methods. *Eng. Anal. Bound. Elem.* **1992**, *10*, 155–160. [CrossRef]
25. Patridge, P.W.; Brebbia, C.A.; Wrobel, L.W. *The Dual Reciprocity Boundary Element Method*; Computational Mechanics Publication: Southampton, UK, 1992.
26. Nowak, A.J.; Neves, A.C. (Eds.) *The Multiple Reciprocity Boundary Element Method*; Computational Mechanics Publication: Southampton, UK, 1994; pp. 1–41.
27. Wei, X.; Huang, A.; Sun, L.L.; Chen, B. Multiple reciprocity singular boundary method for 3D inhomogeneous problems. *Eng. Anal. Bound. Elem.* **2020**, *117*, 212–220. [CrossRef]
28. Chen, W.; Fu, Z.J.; Jin, B.T. A truly boundary-only meshfree method for inhomogeneous problems based on recursive composite multiple reciprocity technique. *Eng. Anal. Bound. Elem.* **2010**, *34*, 196–205. [CrossRef]

29. Fu, Z.J.; Chen, W. A truly boundary-only meshfree method applied to Kirchhoff plate bending problems. *Adv. Appl. Math. Mech.* **2009**, *1*, 341–352.
30. Fu, Z.; Chen, W.; Yang, W. Winkler plate bending problems by a truly boundary-only boundary particle method. *Comput. Mech.* **2009**, *44*, 757–763. [CrossRef]
31. Cheng, A.H.-D.; Antes, H.; Ortner, N. Fundamental solutions of products of Helmholtz and polyharmonic operators. *Eng. Anal. Bound. Elem.* **1994**, *14*, 187–191. [CrossRef]
32. Wang, F.J.; Fan, C.M.; Hua, Q.S.; Gu, Y. Localized MFS for the inverse Cauchy problems of two-dimensional Laplace and biharmonic equations. *Appl. Math. Comput.* **2020**, *364*, 124658. [CrossRef]
33. Fan, C.M.; Li, P.W.; Yeih, W.C. Generalized finite difference method for solving two-dimensional inverse Cauchy problem. *Inverse Probl. Sci. Eng.* **2014**, *23*, 737–759. [CrossRef]